Frequency-Domain Analysis of an Oscillator With an Exceptional Point of Degeneracy

Camilo Moncada, *Student Member, IEEE*, Franco Ramírez, *Senior Member, IEEE*, and Almudena Suárez, *Fellow, IEEE*

***Abstract*— Oscillators based on coupled transmission lines with an exceptional point of degeneracy (EPD) have shown great potential as highly sensitive microwave sensors. However, research into their behavior has thus far been limited to the small-signal regime. In this work, we will perform an in-depth nonlinear analysis using the describing function and harmonic balance (HB) methods. We will begin by deriving a simple EPD condition in terms of the input admittance of the coupled transmission lines. This EPD condition can easily be evaluated using a new graphical method based on representing the zero-value contours of the real and imaginary parts of the oscillator's total admittance, including the active contribution. Moving forward, we will perform an exhaustive calculation of all the periodic and quasi-periodic oscillation modes in the frequency domain and analyze their evolution versus the load resistance. We will demonstrate that there are two different types of quasi-periodic modes, although only one is of interest for the sensing application. A detailed bifurcation analysis will provide valuable insight into the impact of the most relevant parameters on the oscillator's behavior. The circuit has been implemented with two cross-coupled transistors and a Marchand balun, obtaining good experimental results.**

***Index Terms*— Bifurcation, coupled transmission lines, exceptional point of degeneracy (EPD), oscillator, sensor.**

I. Introduction

RECENT works [1], [2], [3], [4], [5], [6], [7], [8], [9], [10], [11], [12] have demonstrated the interest of systems with exceptional points of degeneracy (EPD) for the design of high-sensitivity sensors and efficient radiating array oscillators, among other applications. An EPD occurs [2], [3], [4] when two of more eigenvalues and eigenvectors coalesce at a point of the parameter space. The order of degeneracy agrees with the number of coalescing eigenvalues and eigenvectors [2], [3], [4]. EPDs have been observed in uniform and periodic coupled transmission lines [2], [3], [4], [6], under lossless and gain-to-balance conditions, and coupled resonators [10], under gain-to-loss balance. In those systems, eigenvalue degeneracies lead to eigenvector degeneracies, as demonstrated in [5], [7], and [10]. The EPD is characterized by a high sensitivity to perturbations [5], [7]. In the most usual second-order EPD, the eigenvalues are proportional to the square root of the parameter perturbation [5]. Though nonidealities, such as parasitics and fabrication tolerances, affect the ideal EPD condition, the main properties that characterize this condition are preserved [6], [9], [11].

Gain-to-loss balance implementations have served as a starting point for the design of oscillator circuits [7], [8], [9], [10], [11]. However, for the oscillation to start-up, the small-signal gain must be increased over loss [13]. Despite this unbalance, the square-root sensitivity associated with the second-order EPD is preserved [11], [12]. Different oscillator configurations have been proposed [7], [8], [9], [10], [11], [12]. In single-ladder leaky wave antenna oscillators [8], [9], the gain at the oscillation threshold decreases with the number of cells. In structures based on two coupled *LC* resonators [10], one with gain and the other with loss, the oscillation frequency is very sensitive to the capacitance of each resonator. Among the most sensitive configurations is the one proposed in [11] and [12], based on finite-length coupled transmission lines terminated with balanced gain and loss. The circuit oscillates at two frequencies, whose difference varies with the load resistance and other parameters. In [11], time-domain integration is used to obtain the oscillator waveforms and spectra. However, the analytical investigation is limited to the small-signal stability analysis. In this work, we will address the circuit's nonlinear dynamics. We will analyze its periodic and quasi-periodic modes, as well as the bifurcation phenomena [14] that lead to the desired quasi-periodic solution. This should provide insightful understanding of the oscillator behavior and enable an efficient design. We will depart from the results obtained in [11], which are summarized in the following.

We will consider the oscillator in Fig. 1(a), which was proposed in [11] and [12]. One port in each of the two coupled lines is terminated in a short circuit. The other two ports are terminated in the active-device resistance ($R_N < 0$) and the output load (R_L). The small-signal stability analysis is carried out under the gain-to-loss balance condition $|R_N| = R_L$. It is based on the calculation of the roots of the system characteristic determinant or system poles. Their evolution is analyzed versus $|R_N| = R_L$, i.e., when simultaneously varying

Manuscript received 20 February 2024; revised 10 May 2024; accepted 9 June 2024. This work was supported in part by the Spanish Ministry of Science and Innovation (MCIN/AEI/10.13039/501100011033) under Grant PID2020-116569RB-C31 and in part by the Consejería de Universidades, Igualdad, Cultura y Deporte del Gobierno de Cantabria (Contrato Programa Gobierno de Cantabria—UC). *(Corresponding author: Franco Ramírez.)*

The authors are with the Departamento de Ingeniería de Comunicaciones, Universidad de Cantabria, 39005 Santander, Spain (e-mail: moncadace@unican.es; ramirezf@unican.es; almudena.suarez@unican.es).

Color versions of one or more figures in this article are available at https://doi.org/10.1109/TMTT.2024.3419433.

Digital Object Identifier 10.1109/TMTT.2024.3419433

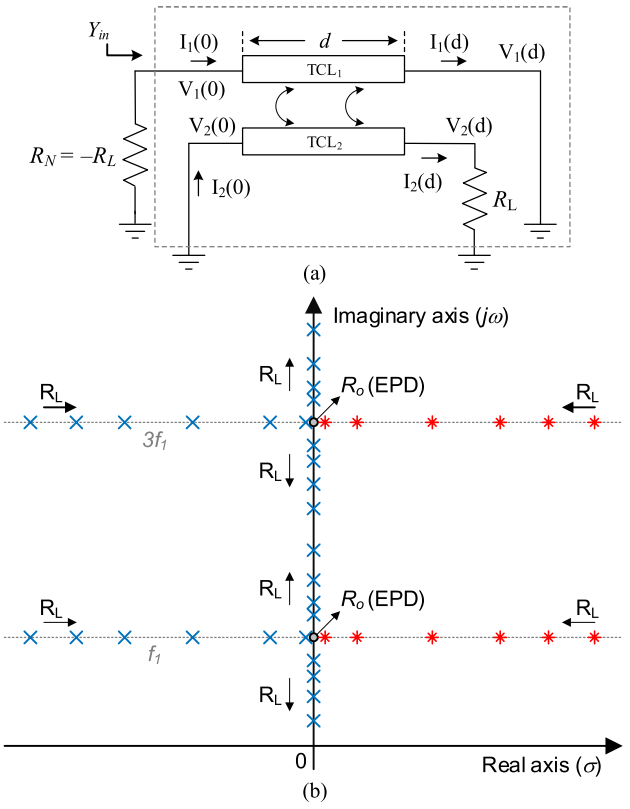

Fig. 1. EPD. (a) Oscillator proposed in [11]. (b) Sketch of the pole variation. Asterisks indicate unstable poles.

the two resistances. For $|R_N| = R_L$ smaller than a certain value R_o, there are pairs of complex-conjugate poles symmetrically located with respect to the imaginary axis [Fig. 1(b)], i.e., with the form $\sigma \pm j\omega_o$ and $-\sigma \pm j\omega_o$. There are also pairs of poles about $(2k+1)\omega_o$, where k is an integer, having the same symmetry but different σ values. As $|R_N| = R_L$ increases, the pairs of poles approach (σ decreases) at constant frequency [Fig. 1(b)] until they merge at the imaginary axis ($\sigma = 0$). This merging occurs at $|R_N| = R_L = R_o$, where two eigenvalues (or poles) and two eigenvectors of the homogeneous system coalesce, which corresponds to the EPD condition. From the EPD, the poles split, and for $|R_N| = R_L > R_o$, they move along the imaginary axis, with the form $0 \pm j(\omega_o \pm \Delta\omega)$. Just after the EPD, the frequency of the poles exhibits a strong variation versus $|R_N| = R_L$ [11], [12], of interest for sensing applications.

Despite the analytical insight provided by the analysis versus $|R_N| = R_L$, the poles on the imaginary axis obtained for $|R_N| = R_L > R_o$ correspond to an unphysical situation. In fact, the (approximate) oscillation start-up condition [13] requires an excess of negative conductance at the resonance frequency. The device must also be nonlinear to achieve steady-state oscillation, so a cubic nonlinearity with the small-signal negative resistance R_N is considered in [11]. The resulting oscillator operates in a quasi-periodic regime, with two incommensurate fundamental frequencies: ω_1 and ω_2, and the frequency difference $\Delta\omega_{21} = |\omega_2 - \omega_1|$ exhibits a strong variation versus R_L. In this work, we will perform an in-depth investigation of the phenomenon that gives rise to this quasi-periodic oscillation, along with a global study of the circuit's oscillation modes and bifurcations [14].

We will initially derive a simple EPD condition in terms of the input admittance of the coupled transmission lines. As demonstrated for the first time to our knowledge, the EPD condition can easily be evaluated through resonance diagrams, in terms of the input admittance. The oscillator solutions will be obtained analytically, with the describing-function approach, and through novel exhaustive methods, based on harmonic balance (HB) [15]. As will be shown, there are two different kinds of periodic and quasi-periodic modes, which are associated with the input susceptance of the coupled structure and its dependence on R_L. We will calculate the bifurcation loci [15], [16], [17] in the space defined by the active resistance R_N and the passive one R_L. This will provide insight into the behavior when deviating from the EPD. The oscillator has been implemented with two cross-coupled transistors and a Marchand balun [18] with very good experimental results.

This article is organized as follows. Section II presents the analytical derivation that leads to a simple EPD condition. Sections III and IV present an exhaustive calculation of the periodic and quasi-periodic oscillation modes, respectively. Section V describes the implementation of a transistor-based oscillator, based on the EPD concept.

II. Small-Signal Analysis of the EPD Oscillator

The analytical study will be based on the circuit in Fig. 2(a). Our initial goal will be the derivation of a simple analytical condition for the occurrence of the EPD, in terms of the input admittance seen from Port 1. Then, we will provide a graphical method for its efficient evaluation through a resonance analysis. We will initially assume that $|R_N| = R_L$. Then, we will consider a fixed value $R_N = -R_o$ and a continuous variation of R_L.

A. Analytical Derivation of the EPD Condition

To obtain the characteristic equation of the circuit in Fig. 1(a), we will apply Kirchoff's laws at Node 1. This implies adding the active admittance $G_N = R_N^{-1}$ and the input admittance Y_{in} of the coupled transmission lines

$$Y_T(G_L, s) = G_N + Y_{\text{in}}(G_L, s) = 0 \tag{1}$$

where $G_L = R_L^{-1}$, s is the complex frequency, and $Y_{\text{in}}(G_L, s)$ is the input admittance when the coupled transmission lines are terminated in $R_L = G_L^{-1}$ [Fig. 2(a)].

Note that because the analysis is carried out in terms of admittances, the equations will be expressed in terms of G_N and G_L, instead of R_N and R_L. However, in the text, we will refer to both conductance and resistance. From [11] and [12], under $|R_N| = R_L > R_o$ (where R_o corresponds to the EPD), there should be several pairs of complex-conjugate poles on the imaginary axis [Fig. 1(b)]. These poles will have the form

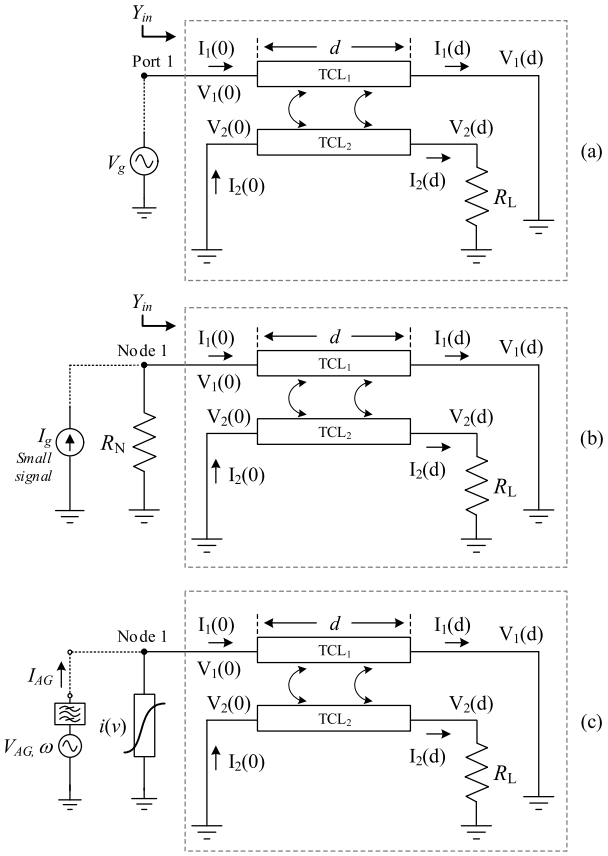

Fig. 2. Oscillator loaded with a pair of coupled transmission lines. (a) Calculation of the input admittance of the coupled transmission lines under loaded conditions. (b) Schematic for the small-signal analysis. (c) Schematic for the nonlinear oscillator analysis. It includes the AG used for the calculation of the periodic solutions.

$s = \pm j\omega$, so replacing $s = j\omega$ in (1) and splitting into real and imaginary parts, we obtain

$$\begin{aligned} G_T(G_L,\omega) &= G_N + Y_{\text{in}}^r(G_L,\omega) \\ &= -G_L + Y_{\text{in}}^r(G_L,\omega) = 0, \qquad (2a) \\ B_T(G_L,\omega) &= Y_{\text{in}}^i(G_L,\omega) = 0 \qquad (2b) \end{aligned}$$

where superscripts r and i indicate the real and imaginary parts, respectively. This has also been made of $|R_N| = R_L$ or, equivalently, $|G_N| = G_L$. From simple inspection, to fulfill (2), Y_{in}^r must agree with the load conductance G_L when $Y_{\text{in}}^i = 0$. To calculate Y_{in}, we will excite the coupled transmission lines with the auxiliary voltage source V_g [Fig. 2(a)] at the frequency ω. As in [11] and [12], in our analytical study, the coupled transmission lines will be assumed lossless and dispersion-less. This will be fundamental for achieving analytical insight. Making use of the transmission matrix of the coupled transmission lines, we can express [11]

$$\begin{bmatrix} V_g \\ 0 \\ I_1(0) \\ I_2(0) \end{bmatrix} = \exp\left(j\omega\left[M_{\text{par}}\right]d\right) \begin{bmatrix} 0 \\ R_L I_2(d) \\ I_1(d) \\ I_2(d) \end{bmatrix} \qquad (3)$$

where d is the total line length and the matrix $[M_{\text{par}}]$ describes coupled transmission lines in terms of their inductances and capacitances per unit length. It is given by

$$\begin{aligned} M_{\text{par}} &= \begin{bmatrix} 0 & [L_{\text{mat}}] \\ [C_{\text{mat}}] & 0 \end{bmatrix}, \quad L_{\text{mat}} = \begin{bmatrix} L_0 & L_m \\ L_m & L_0 \end{bmatrix} \\ C_{\text{mat}} &= \begin{bmatrix} C_0 + C_m & -C_m \\ -C_m & C_0 + C_m \end{bmatrix}. \qquad (4) \end{aligned}$$

To obtain the elements of the transmission matrix $\exp(j\omega[M_{\text{par}}]d)$, we will first express it as

$$\exp\left(j\omega\left[M_{\text{par}}\right]d\right) = \Lambda\left[\text{diag}\left(e^{j\omega(\lambda_{M_{\text{par}}})d}\right)\right]\Lambda^{-1} \qquad (5)$$

where $\lambda_{M_{\text{par}}}$ is the set of eigenvalues of $[M_{\text{par}}]$ and Λ is the matrix composed of its eigenvectors. The eigenvalues are

$$\lambda_{M_{\text{par}}} = \text{eig}\left(M_{\text{par}}\right) = \begin{bmatrix} \beta & \alpha & -\beta & -\alpha \end{bmatrix}^T \qquad (6)$$

where

$$\alpha = \sqrt{C_0(L_0 + L_m)};\ \beta = \sqrt{(C_0 + 2C_m)(L_0 - L_m)}. \qquad (7)$$

The matrix Λ with the eigenvectors of $[M_{\text{par}}]$ in its columns is

$$\Lambda = \begin{bmatrix} \frac{-\alpha}{C_0} & \frac{-\beta}{(C_0+2C_m)} & \frac{\beta}{(C_0+2C_m)} & \frac{\alpha}{C_0} \\ \frac{-\alpha}{C_0} & \frac{\beta}{(C_0+2C_m)} & \frac{-\beta}{(C_0+2C_m)} & \frac{\alpha}{C_0} \\ 1 & -1 & -1 & 1 \\ 1 & 1 & 1 & 1 \end{bmatrix}. \qquad (8)$$

Now, the input admittance Y_{in} can be calculated from (3) as

$$Y_{\text{in}}(G_L,\omega) = \frac{I_1(0)}{V_g} \qquad (9)$$

which can be expressed as a single quotient

$$\begin{aligned} &Y_{\text{in}}(G_L,\omega) \\ &= \frac{\left[R_L\left(\left(2PC_\alpha + 2PC_\beta\right)^2 - 4\left(HS_\beta - NS_\alpha\right)\left(QS_\alpha - TS_\beta\right)\right) + 8Pj\left(HC_\alpha S_\beta + NC_\beta S_\alpha\right)\right]}{R_L\left(8Pj\left(HC_\alpha S_\beta + NC_\beta S_\alpha\right)\right) - 16HNS_\alpha S_\beta} \end{aligned} \qquad (10)$$

where we have introduced the terms

$$\begin{aligned} P &= \frac{1}{4}, \quad Q = \frac{1}{4}\frac{C_0}{\alpha}, \quad N = \frac{1}{4}\frac{\alpha}{C_0}, \\ T &= \frac{1}{4}\frac{(C_0+2C_m)}{\beta}, \quad H = \frac{1}{4}\frac{\beta}{(C_0+2C_m)}. \qquad (11) \end{aligned}$$

On the other hand, C_α, S_α, C_β, and S_β are compact expressions of the following trigonometric functions:

$$\begin{aligned} C_\alpha &= \cos(d\alpha\omega), \quad S_\alpha = \sin(d\alpha\omega) \\ C_\beta &= \cos(d\beta\omega), \quad S_\beta = \sin(d\beta\omega). \qquad (12) \end{aligned}$$

For an insightful analysis, we will distinguish the terms of Y_{in} that are dependent and independent of the load resistance R_L. This distinction will be key for the insightful calculation of the oscillator solutions.

When splitting Y_{in} into real and imaginary parts, we obtain

$$\begin{aligned} Y_{\text{in}}(G_L,\omega) &= Y_{\text{in}}^r + jY_{\text{in}}^i \\ &= \frac{(-64T_{r1}T_{r2})R_L + j(-8T_{i1}T_{i2}(R_L))}{(4T_{s1})R_L^2 + T_{s2}} \qquad (13) \end{aligned}$$

where

$$
\begin{aligned}
T_{r1} &= HS_\beta - NS_\alpha \\
T_{r2} &= H\left(NTS_\alpha S_\beta^2 - NQS_\alpha^2 S_\beta - P^2 C_\alpha^2 S_\beta\right) + NP^2 C_\beta^2 S_\alpha \\
T_{i1} &= HC_\alpha S_\beta + NC_\beta S_\alpha \\
T_{i2} &= \left[P^2\left(C_\alpha + C_\beta\right)^2 - \left(HS_\beta - NS_\alpha\right)\left(QS_\alpha - TS_\beta\right)\right]R_L^2 \\
&\quad + 4HNS_\alpha S_\beta \\
T_{s1} &= \left(HC_\alpha S_\beta + NC_\beta S_\alpha\right)^2 \\
T_{s2} &= 256H^2N^2S_\alpha^2 S_\beta^2.
\end{aligned} \tag{14}
$$

We emphasize that (13) and (14) are only valid under the assumption of lossless and nondispersive coupled lines. The only term in (14) depending on R_L is T_{i2}. To solve system (2), we will first pay attention to $B_T(G_L, \omega) = Y_{\text{in}}^i = 0$. The numerator of Y_{in}^i in (13) is the product of two factors: T_{i1}, which only depends on ω, and T_{i2}, which depends on both ω and R_L. Because T_{i1} does not depend on R_L, this term cannot be responsible for the occurrence of the EPD, obtained at a particular R_L. Thus, we should pay attention to $T_{i2}(\omega, R_L) = 0$. It is explicitly written as

$$
T_{i2}(\omega, R_L) = T_{i.21}(\omega)R_L^2 + T_{i.22}(\omega) = 0 \tag{15}
$$

where

$$
\begin{aligned}
T_{i.21} &= P^2\left(C_\alpha + C_\beta\right)^2 - \left(HS_\beta - NS_\alpha\right)\left(QS_\alpha - TS_\beta\right) \\
T_{i.22} &= 4HNS_\alpha S_\beta
\end{aligned}
$$

Solving for R_L, one obtains

$$
R_L^2 = -\frac{T_{i22}(\omega)}{T_{i21}(\omega)}. \tag{16}
$$

The above function provides a continuous set of values (ω, R_L) that fulfill $Y_{\text{in}}^i = 0$. The poles will be on the imaginary axis if the pair (ω, R_L) also satisfies (2a). This implies that $Y_{\text{in}}^r = G_L = R_L^{-1}$ or equivalently

$$
Y_{\text{in}}^r(G_L, \omega) - G_L = 0. \tag{17}
$$

Replacing the expression of $Y_{\text{in}}^r(G_L, \omega)$ [see (13)]

$$
\frac{(-64T_{r1}T_{r2})R_L}{(4T_{s1})R_L^2 + T_{s2}} - \frac{1}{R_L} = 0. \tag{18}
$$

Next, we will introduce in (18) R_L that fulfills both $B_T(G_L, \omega) = Y_{\text{in}}^i = 0$ and $T_{i2}(\omega, R_L) = 0$, given by (16). Making use of the full expressions of the functions (P, Q, N, H, and T) and (C_α, C_β, S_α, and S_β), the two terms on the left-hand side (LHS) of (18) cancel each other out. The resulting zero value is independent on the frequency ω at which (16) is fulfilled. Thus, provided that (16) [or equivalently (2b) under $T_{i2}(\omega, R_L) = 0$] is satisfied, (18) [or equivalently (2a)] is satisfied too. There is a limit ω value for the fulfillment of (16), i.e., for the presence of the pairs of poles $s = \pm j\omega$ on the imaginary axis. This corresponds to a minimum of the function $R_L^2(\omega)$, given by

$$
\frac{\partial R_L^2}{\partial \omega} = \frac{-\frac{\partial T_{i22}(\omega)}{\partial \omega}T_{i21}(\omega) + T_{i22}(\omega)\frac{\partial T_{i21}(\omega)}{\partial \omega}}{T_{i21}^2(\omega)} = 0 \tag{19}
$$

which agrees with the EPD condition. Solving for ω from (19) and replacing it in (18), one obtains the EPD, given by (ω_o, R_o).

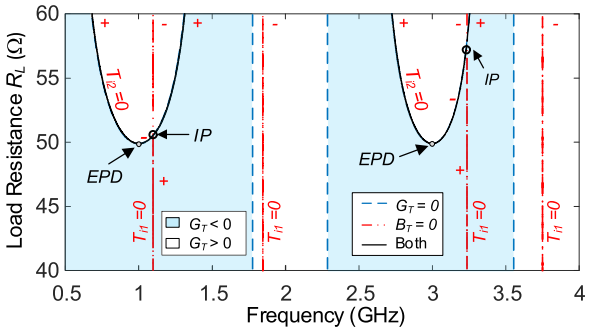

Fig. 3. Resonance analysis (under small-signal conditions) versus R_L, carried out by tracing the two zero-value contours $G_T(G_L, \omega) = 0$ and $B_T(G_L, \omega) = 0$ in the plane (ω, R_L). The sections with negative conductance ($G_T < 0$) are shadowed and the sign of $\partial B_T/\partial \omega$ is indicated with + or −.

B. Graphical Determination of the EPD

Using the results of Section II-A, it will be possible to carry out a simple graphical calculation of the EPD by tracing the zero-value contours $G_T(G_L, \omega) = 0$ and $B_T(G_L, \omega) = 0$ in the plane defined by ω and R_L. To illustrate this, we will consider the following inductances and capacitances per unit length [11]: $L_0 = 480$ nH/m, $L_m = 367.4$ nH/m, $C_0 = 57.9$ pF/m, and $C_m = 102.7$ pF/m. Fig. 3 shows the resulting contours $G_T(G_L, \omega) = 0$ and $B_T(G_L, \omega) = 0$. Note that there are two sets of contours: about 1 and 3 GHz. We will initially focus on the behavior about $f_o = 1$ GHz. The contour $B_T = \text{Im}[Y_{\text{in}}(G_L, \omega)] = 0$ is composed of a bell-shaped curve, corresponding to $T_{i2}(\omega, R_L) = 0$, and a vertical straight line, corresponding to $T_{i1}(\omega) = 0$, since T_{i1} does not depend on R_L. The contour $G_T = 0$ is also given by a bell-shaped curve and a vertical straight line. The bell-shaped curves providing $G_T = 0$ and $B_T = T_{i2}(\omega, R_L) = 0$ overlap. This is because, as shown in Section II-A, $T_{i2}(\omega, R_L) = 0$ implies that $G_T(G_L, \omega) = 0$. In contrast, the straight lines providing $G_T = 0$ and $B_T = T_{i1}(\omega) = 0$ are different. The behavior is analogous about 3 GHz and other odd harmonic frequencies. The EPD is obtained at the minimum of the bell-shaped curve, which fulfills the condition $\partial R_L/\partial \omega = 0$.

The contours in Fig. 3 (both the bell-shaped curves and the straight lines) delimit the regions of the plane (ω, R_L) providing negative/positive total conductance (G_T) and susceptance (B_T). Regions with $G_T < 0$ are shadowed. The sign of the frequency derivative $\partial B_T/\partial \omega$ is indicated through $B_T = 0$. Note that there is an intersection point (IP) between the straight line and the bell-shaped curve. Through the vertical line, the sign of $\partial B_T/\partial \omega$ is positive below IP and negative above IP. Through the bell-shaped curve, the sign of $\partial B_T/\partial \omega$ is positive (negative) on the left side (right side) between the EPD and the IP. Above IP, the sign of $\partial B_T/\partial \omega$ is positive on both sides.

We conclude that for any pair of coupled transmission lines, with arbitrary parameters, we can obtain the EPD (ω_o, R_o) simply by tracing the zero-value contours $G_T(G_L, \omega) = 0$ and $B_T(G_L, \omega) = 0$ in the plane (ω, R_L). The EPD corresponds to the minimum of the bell-shaped curve, $\partial R_L/\partial \omega = 0$.

The resonance diagram will be compared with the results of a rigorous stability analysis of the dc solution. It will be carried

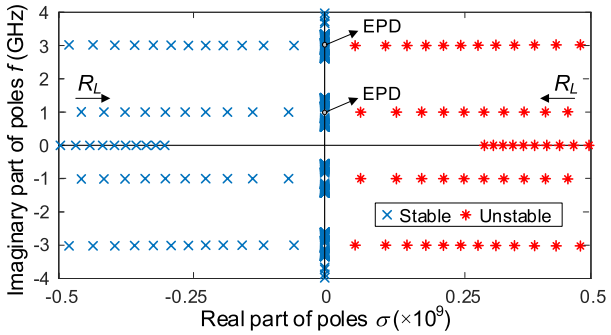

Fig. 4. Simultaneous variation of R_N and R_L, with $|R_N| = R_L$. Stability analysis of the dc solution through the application of pole-zero identification to an impedance-type transfer function. This is calculated at Node 1, using the small-signal current source shown in Fig. 2(b). Asterisks indicate unstable poles.

out by applying pole-zero identification to an impedance-type transfer function [19], [20]. This is obtained by connecting a small-signal current source I_g in parallel at the analysis node [Node 1 in Fig. 2(b)] and calculating the ratio between the node voltage and the current introduced [19], [20]. The results are shown in Fig. 4. For $R_L < R_o$, there are several pairs of complex-conjugate poles on both the right-hand side of the complex plane (RHS) and the LHS, at 1 and 3 GHz. The poles in the RHS are consistent with the resonances associated with $T_{i1}(\omega) = 0$ in Fig. 3, which fulfill $G_T < 0$ and $\partial B_T/\partial\omega > 0$, corresponding to the approximate oscillation start-up conditions [13]. Note that, for each pair of complex-conjugate poles at $\sigma \pm j\omega$, there is another pair $-\sigma \pm j\omega$. When R_L increases, they approach the imaginary axis at a constant frequency until they merge on the imaginary axis ($\sigma = 0$) for $R_L = R_o$, which corresponds to the EPD. After the EPD, they split into two pairs of complex-conjugate poles with zero real part $\pm j\omega$ (located on the imaginary axis). For $R_L > R_o$, they move along the imaginary axis. This is consistent with the overlap of the bell-shaped curves $G_T(G_L, \omega) = 0$ and $B_T(G_L, \omega) = 0$ in Fig. 3. Remember that, when evaluated in terms of s, the total admittance function $Y_T(G_L, s) = 0$ agrees with the characteristic equation [see (1)]. Thus, the conditions $G_T(G_L, \omega) = 0$ and $B_T(G_L, \omega) = 0$ imply the fulfillment of the characteristic equation for $s = \pm j\omega$. For each R_L above the minimum of the bell-shaped curve, the characteristic equation is fulfilled for $s = \pm j\omega_1$ and $s = \pm j\omega_2$. This implies that there are two pairs of poles on the imaginary axis. When reducing R_L toward the minimum of the bell-shaped curve, obtained for R_o, the two pairs of poles approach each other and finally merge at R_o. At that point, the two pairs of poles ($\pm j\omega_1$ and $\pm j\omega_2$) merge into two pairs of repeated poles $\pm j\omega_o$, which corresponds to the EPD condition.

C. Variation of G_L at Constant G_N

For the oscillation to start-up, the absolute value of the negative conductance of the active device must exceed that of the passive load under small signal [13] at the analysis node. Moreover, the element that provides G_N must be implemented with a diode or transistor(s), so a simultaneous variation of $|G_N| = G_L$ (or, equivalently, $|R_N| = R_L$) will not be possible in practice. In the following analysis, we will set G_N to the EPD value ($G_N = -1/R_o$). This can only be done approximately since an (ideal) infinite number of decimal figures would be needed. The EPD value considered is $R_o = 49.88\ \Omega$ [11], [12], which agrees with the one obtained from Fig. 3. The resulting bell-shaped curves $G_T(G_L, \omega) = 0$ and $T_{i2}(\omega, R_L) = 0$ [Fig. 5(a)] are no longer overlapping. However, they are ideally tangential at (ω_o, R_o) and about $[(2k+1)\omega_o, R_o]$. The regions where $G_T(G_L, \omega) < 0$ are shadowed in Fig. 5(a) and the sign of $\partial B_T/\partial\omega$ is indicated.

Fig. 5(b) shows the pole locus when increasing R_L from 20 to 80 Ω and Fig. 5(c) shows an expanded view about $f_o = 1$ GHz. The form of variation of the poles has changed with respect to Fig. 4. For $R_L < R_o$, there are still two pairs of complex-conjugate poles with the same imaginary part $\omega = \pm\omega_o$ on the LHS and the RHS. However, now, they are not symmetrical about the imaginary axis. As R_L increases, they approach each other, and at $R_L = R_o$, they ideally meet on the imaginary axis. This meeting point cannot be obtained in the numerical analysis since $G_N = -1/R_o$ cannot be set to the exact EPD value. When further increasing R_L, one of the pairs shifts leftward and then crosses the imaginary axis to the RHS in a direct Hopf bifurcation ($H_{I,1}$) [14], [21]. The other pair shifts rightward onto the RHS. Unlike the case of Fig. 4, for $R_L > R_o$, the poles do not remain on the imaginary axis. However, there is still a strong variation of their imaginary part (frequency ω) versus R_L. To further illustrate the interest of the resonance analysis, we have considered a more accurate model of the coupled transmission lines, including losses and dispersion [22]. Under these two effects, the EPD is no longer observed. To recover the EPD, we have introduced an inductor L in parallel at the analysis node. We have tuned L and R_N until obtaining a tangency of the two contours $G_T(G_L, \omega) = 0$ and $T_{i2}(\omega, R_L) = 0$ at the minimum of the bell-shaped curve, which is achieved for $L = 0.29\ \mu$H and $R_N = 48.5\ \Omega$ [Fig. 5(d)]. The high L value is because we only require a relatively small correction in susceptance $-1/(L\omega)$. As in the ideal case of Fig. 5(a), the loci of $G_T(G_L, \omega) = 0$ and $B_T(\omega, R_L) = 0$ are tangent at the minimum of the two curves, which has the same geometrical implications. Thus, it necessarily gives rise to the same degeneracy.

III. Calculation of the Periodic Oscillation Modes

We will perform, for the first time to our knowledge, an exhaustive calculation of the periodic oscillation modes of the EPD oscillator versus the load resistor R_L. Though the circuit is expected to operate in quasi-periodic regime, a previous determination of these modes will facilitate the understanding of the solution-curve pattern. The modes will initially be calculated in an analytical manner using the describing function [23]. The results will be compared with those obtained with commercial HB (Keysight ADS [24]) and a contour-intersection method, based on HB [15], which exhaustively provides all the coexisting periodic modes.

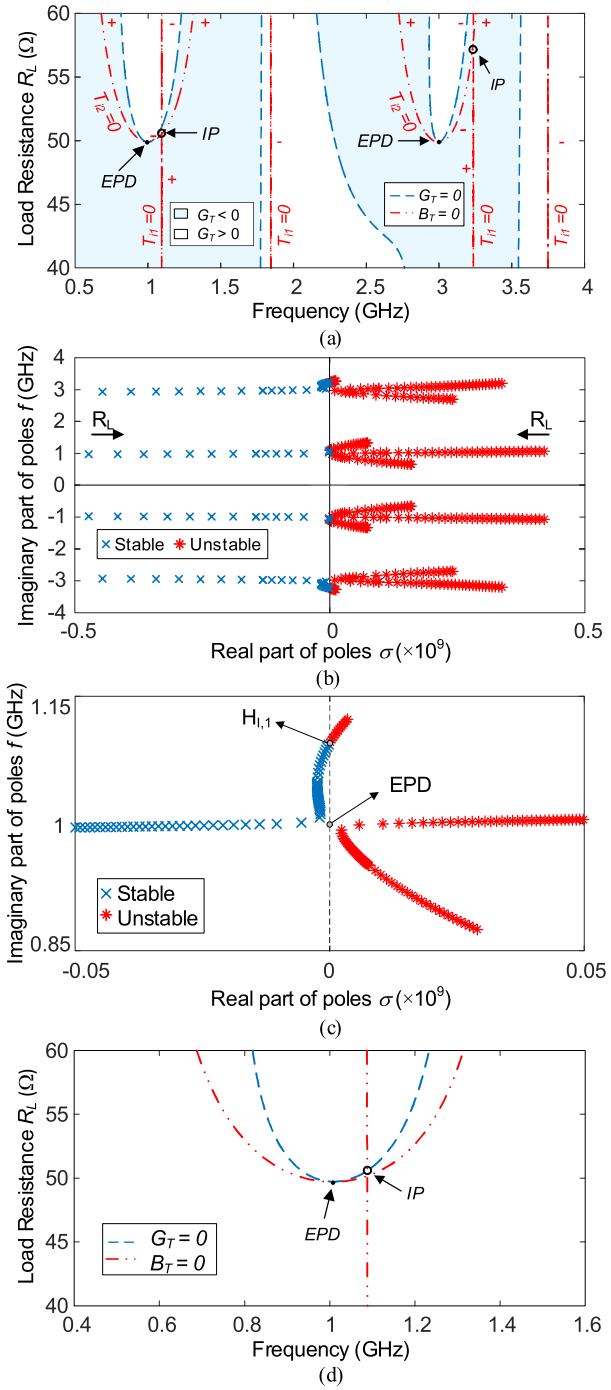

Fig. 5. Stability analysis when considering a constant active-device conductance $G_N = -1/R_o$ and varying the load resistance R_L. (a) Zero-value contours $G_T(G_L, \omega) = 0$ and $B_T(G_L, \omega) = 0$ in the plane defined by ω and R_L. The sections with negative conductance are shadowed and the sign of $\partial B_T/\partial\omega$ is indicated with + or −. (b) Pole locus. Asterisks indicate unstable poles. (c) Expanded view about 1 GHz. (d) Resonance curves in the presence of losses and dispersion. We have tuned an inductor L, in parallel at the analysis node, and R_N to recover the EPD.

A. Analytical Calculation of the Solution Curves

As in [11], the active device is modeled with a cubic nonlinearity $i = G_N v + bv^3$. Its one-tone describing function [21] is the ratio between the fundamental component of the current $i(t)$ and the excitation voltage amplitude V. This provides $G(V) = G_N + 3bV^2/4$. To formulate the oscillator at the fundamental frequency ω, we apply Kirchoff's laws at Node 1 [Fig. 2(c)]. The resulting complex equation, derived from the total admittance function, is

$$\begin{aligned} Y_T &= G(V) + Y_{\text{in}}(R_L, d, \omega) \\ &= G_N + \frac{3}{4}bV^2 + \frac{(-64T_{r1}T_{r2})R_L + j(-8T_{i1}T_{i2})}{(4T_{s1})R_L^2 + T_{s2}} = 0. \end{aligned} \tag{20}$$

Next, we split (20) into the real and imaginary parts

$$G_T = G_N + \frac{3}{4}bV^2 + \frac{(-64T_{r1}T_{r2})R_L}{(4T_{s1})R_L^2 + T_{s2}} = 0 \tag{21a}$$

$$B_T = T_{i1}(\omega)T_{i2}(\omega, R_L) = 0. \tag{21b}$$

The solutions of (21) provide the amplitude and frequency of the steady-state periodic oscillations. In terms of frequency, we can have two types of solutions: Type-I solutions, when $T_{i1}(\omega) = 0$ in (21b), and Type-II solutions, when $T_{i2}(\omega, R_L) = 0$ in (21b).

The Type-I solution curve(s) will exhibit a constant oscillation frequency versus R_L, obtained from $T_{i1}(\omega) = 0$ (the straight line of Fig. 3) in this approximate analysis. From (21a), the steady-state amplitude V will vary versus R_L as

$$V = 2\sqrt{\frac{\left(-G_N + \frac{(64T_{r1}T_{r2})R_L}{(4T_{s1})R_L^2+T_{s2}}\right)}{3b}}. \tag{22}$$

The functions T_{r1}, T_{r2}, T_{s1}, and T_{s2} depend on ω but do not depend on R_L [see (14)]. In (22), they should be evaluated at the frequency fulfilling $T_{i1}(\omega) = 0$. Thus, they take constant values. The amplitude V will decrease with R_L until reaching $V = 0$.

The Type-II solutions exhibit both frequency and amplitude dependence on R_L. The oscillation frequency fulfills $T_{i2}(\omega, R_L) = 0$, Thus, in this approximate analysis, its value will lie on the already calculated bell-shaped curve. As demonstrated in Section II-A, when the condition $T_{i2}(\omega, R_L) = 0$ is fulfilled, we have $\text{Re}[Y_{\text{in}}(R_L, d, \omega)] = G_L$. Thus, the steady-state amplitude V of Type-II solutions will vary versus R_L as

$$V = 2\sqrt{\frac{-G_N - 1/R_L}{3b}}. \tag{23}$$

This amplitude, which does not depend on the oscillation frequency, will increase with R_L and saturate.

Fig. 6 shows the frequency and amplitude of the two types of solutions, traced versus R_L when considering $R_N = -49.88$ Ω. The Type-I solution curve exhibits a constant frequency $f_o = 1$ GHz. It departs from the amplitude $V = 0.95$ V at $R_L = 40$ Ω, which decays to zero ($V = 0$ V) at the inverse Hopf bifurcation $H_{I,1}$, already detected in the stability analysis of Fig. 5(c). Thus, the two independent analyses are consistent.

We will now consider the solution curves of Type II. As seen in Fig. 6(a), their oscillation frequencies (ω_1 and ω_2) agree with those on the left and right sides of the bell-shaped curve $T_{i2}(\omega, R_L) = 0$. The amplitude V is the same for the two

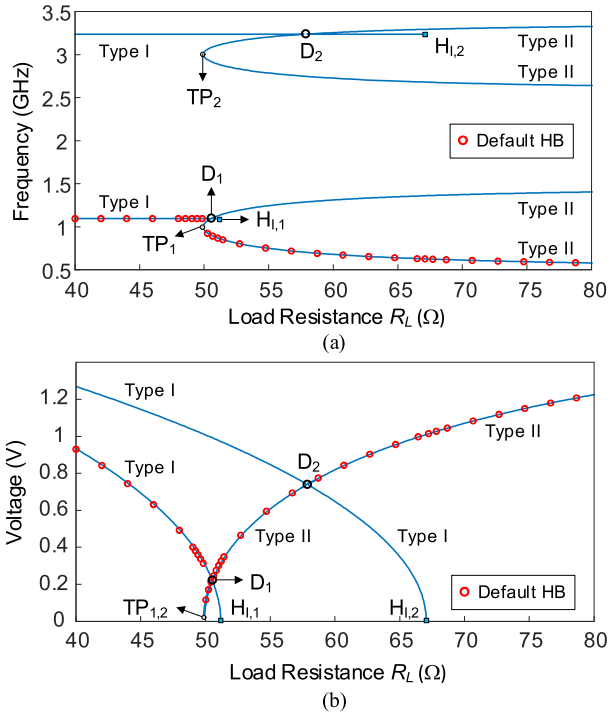

Fig. 6. Periodic oscillation modes versus R_L obtained with the analytical system (22). The results are validated with an oscillator analysis in commercial HB, denoted as "Default HB." (a) Frequency. (b) Amplitude.

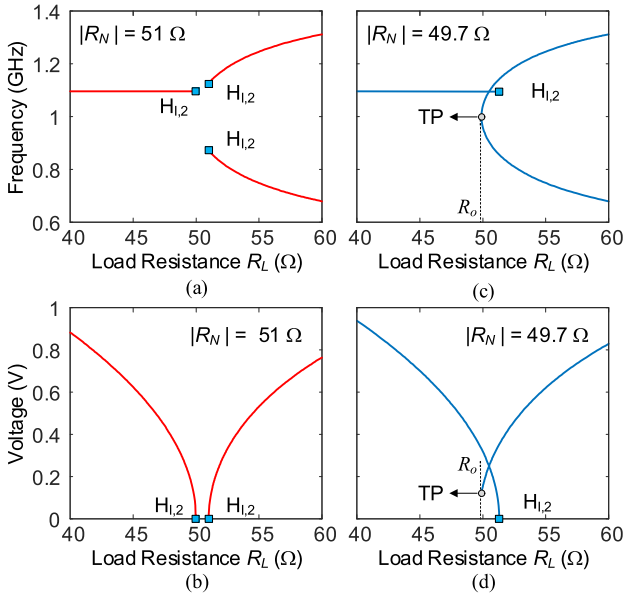

Fig. 7. Solution curves for the two different cases $|R_N| > R_o$ and $|R_N| < R_o$. (a) and (b) Frequency and amplitude for $R_N = -51\ \Omega$, fulfilling $|R_N| > R_o$. (c) and (d) Frequency and amplitude for $R_N = -49.7\ \Omega$, fulfilling $|R_N| < R_o$.

oscillations (at ω_1 and ω_2), as shown in Fig. 6(b). For a better understanding, we will slightly vary the negative resistance R_N (as an additional parameter) about the EPD value R_o. We will consider two cases: $|R_N| > R_o$ and $|R_N| < R_o$.

For $|R_N| > R_o$, we obtain two curves with different frequencies and overlapping amplitudes. See Fig. 7(a) and (b), where we have considered $R_N = -51\ \Omega$. The two curves start from $V = 0$, in a double-Hopf bifurcation. At this bifurcation, the two frequencies, ω_1 and ω_2, are different and agree with the two roots of $T_{i2}(\omega, R_L) = 0$ at $R_L = -R_N$.

For $|R_N| < R_o$, we obtain a single oscillation curve with a turning point (TP), occurring at $V \neq 0$, for $R_L = R_o$ and $\omega_1 = \omega_2 = \omega_o$ (minimum of the bell-shaped curve). See Fig. 7(c) and (d), where we have considered $R_N = -49.9\ \Omega$. As R_L increases from the TP, the frequencies ω_1 and ω_2 gradually separate, following the bell-shaped curve, whereas the amplitudes of the two sections remain overlapping. Note that setting the precise value $R_N = R_o$ is impossible in practice. If this ideal value were reached, we would have a single oscillation curve with two sections starting from $V = 0$ at $\omega_1 = \omega_2 = \omega_o$ in a degenerate double-Hopf bifurcation.

The behavior about 3 GHz is analogous (Fig. 6). However, the solutions of Type I have a different amplitude from those at 1 GHz since T_{r1}, T_{r2}, T_{s1}, and T_{s2} in (22) are frequency dependent. On the other hand, the amplitude of the solutions of Type II overlaps that obtained at 1 GHz since this amplitude does not depend on ω, as seen in (23).

The results obtained with the analytical formulation have been validated with an oscillator analysis in commercial HB [24], referred to here as "Default HB." For the comparison, we have considered only the fundamental frequency (number of harmonic terms (NH) = 1). The corresponding solution points, represented with red circles in Fig. 6, overlap the analytical predictions. However, commercial HB is unable to predict the coexisting solution curves. When sweeping a parameter (such as R_L in Fig. 6), it tries to find a solution at each new parameter value, regardless of the possible folding of the solution curve. Convergence problems often arise near the folding point. However, there can also be a jump to a distinct solution curve if it is close enough for the error-minimization algorithm to converge to it. At $R_L = 49.8\ \Omega$, it jumps from the solution curve of Type I to the solution curve of Type II. This jump prevents the correct interpretation of the curve pattern.

B. Bifurcation Analysis

At Hopf bifurcations, the amplitude of the periodic oscillations tends to zero [21], [25]. Solutions of Type I and Type II have different amplitude expressions, given by (22) and (23), respectively. Thus, we can expect two different Hopf-bifurcation loci. The first Hopf locus (Hopf-I) is associated with periodic solutions of Type I. To obtain this locus, we set $V = 0$ in (22) and also use the resonance condition $T_{i1}(\omega) = 0$

$$V = 0 = 2\sqrt{\frac{\left(-1/R_N + \frac{(64T_{r1}T_{r2})R_L}{(4T_{s1})R_L^2 + T_{s2}}\right)}{3b}} \tag{24a}$$

$$T_{i1}(\omega) = 0. \tag{24b}$$

The above system of two real equations in the three variables R_N, R_L, and ω provides the locus Hopf-I. The equation $T_{i1}(\omega) = 0$ only has one solution in ω. Replacing it in (24a), we obtain

$$R_N = \frac{(4T_{s1})R_L^2 + T_{s2}}{(64T_{r1}T_{r2})R_L}. \tag{25}$$

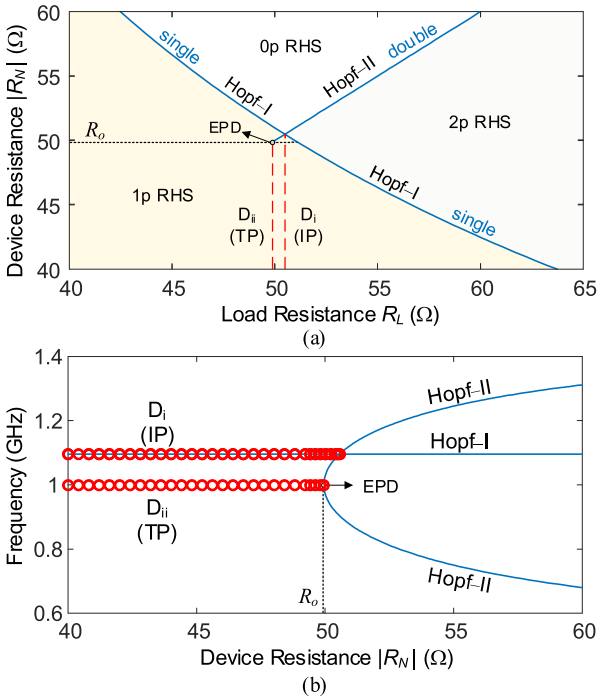

Fig. 8. Bifurcation loci. There are two types of Hopf loci (Hopf-I and Hopf-II) and two types of D-bifurcation loci (D_i and D_{ii}). (a) Representation in the plane $(R_L, |R_N|)$. (b) Representation in the plane $(|R_N|, \omega)$.

In the plane $(R_L, |R_N|)$, (25) provides the locus Hopf-I, traced in Fig. 8(a). Its constant frequency is represented versus $|R_N|$ in Fig. 8(b). When crossing Hopf-I, a single pair of complex-conjugate poles of the dc solution crosses the imaginary axis at the frequency root of $T_{i1}(\omega) = 0$ [Fig. 8(b)].

To obtain the second Hopf locus (Hopf-II), associated with periodic solutions of Type II, we set $V = 0$ in (23). We also impose the resonance condition $T_{i2}(\omega, R_L) = 0$

$$R_N = -R_L \tag{26a}$$

$$T_{i2}(\omega, R_L) = 0. \tag{26b}$$

As (26b) does not depend on R_N, the locus Hopf-II will provide the straight line (26a) in the plane defined by R_L and $|R_N|$. The frequency ω varies through the locus following (26b), i.e., the bell-shaped curve. Thus, the locus Hopf-II is composed of very particular bifurcations, at which two pairs of complex-conjugate poles cross the imaginary axis simultaneously in either the same sense or opposite senses.

The two Hopf loci represented in Fig. 8 divide the plane (R_L, R_N) into three regions: with one pair of poles on the RHS, with zero poles on the RHS, and with two pairs of poles on the RHS. The EPD is the limit point of Hopf-II. Between the EPD and the intersection between the two Hopf loci, there is a pair of poles crossing to the LHS and another pair of poles crossing to the RHS simultaneously. This does not affect the pole count.

A D-type bifurcation [17], [21] is obtained when the Jacobian matrix of the steady-state equations becomes singular. In our case, the D-type bifurcations are defined by the singularity of the Jacobian matrix of system (21)

$$\det(V, \omega) = \begin{vmatrix} \frac{\partial G_T}{\partial V} & \frac{\partial G_T}{\partial \omega} \\ \frac{\partial B_T}{\partial V} & \frac{\partial B_T}{\partial \omega} \end{vmatrix} = \begin{vmatrix} \frac{3}{2} bV & \frac{\partial \left(\frac{(-64 T_{r1} T_{r2}) R_L}{(4T_{s1}) R_L^2 + T_{s2}} \right)}{\partial \omega} \\ 0 & \frac{\partial (T_{i1} T_{i2})}{\partial \omega} \end{vmatrix} = 0 \tag{27}$$

where "det" means determinant. Assuming that $V \neq 0$, the D-type bifurcation condition is

$$\frac{\partial [T_{i1}(\omega) T_{i2}(R_L, \omega)]}{\partial \omega} = 0 \tag{28}$$

which must be fulfilled together with the steady-state equations (21). This can occur under two different situations: 1) when both $T_{i1}(\omega) = 0$ and $T_{i2}(R_L, \omega) = 0$ and 2) when $T_{i2}(R_L, \omega) = 0$ and $\partial T_{i2}(R_L, \omega)/\partial \omega = 0$. We will have 1) at the intersection between the Type-I and Type-II periodic curves of Fig. 6. The corresponding locus, denoted as D_i, has been represented in Fig. 8 in the two planes $(R_L, |R_N|)$ and $(|R_N|, \omega)$. We will have 2) at the TP of the solution curves of Type II (Fig. 7). This is obtained for $|R_N| \leq R_o$ and the frequency at TP agrees with the minimum of the bell-shaped curve. The corresponding locus, denoted as D_{ii}, is also represented in Fig. 8. The EPD corresponds to the co-dimension two bifurcations at which Hopf-II and D_{ii} meet. It provides two degenerate periodic solutions with amplitude $V = 0$ and the same fundamental frequency ω_o. This result is consistent with the independent stability analysis of the dc solution [Fig. 5(c)].

C. Exhaustive HB Analysis of Periodic Solutions

In this section, we will compare the results of the describing-function analysis with those obtained with HB, under NH = 7 harmonic terms. To exhaustively calculate all the oscillation modes, we will make use of the contour intersection method proposed in [15]. This is based on the introduction into the circuit of a voltage auxiliary generator (AG) at the frequency ω, with the voltage amplitude V_{AG} [Fig. 2(c)]. It is connected in parallel at the analysis node, with an ideal bandpass filter at ω.Without the bandpass filter, the voltage AG would short-circuit frequencies different from the fundamental one. The conditional sentence is [24]: "RAG = if abs(freq − fAG) < 100 Hz, then 1e-18 else 1e18 endif." The aim of the AG is to obtain a nonlinear admittance function, defined as the ratio between the AG current I_{AG} and voltage: $Y_{AG}(V_{AG}, \omega) = 0$. To extract this function, we perform a double sweep in ω and V_{AG} and carry out an HB simulation with NH = 7 (or any other suitable number) at each sweep step. Then, all the coexisting solutions are given by the intersections of the two following zero-value contours:

$$\begin{aligned} \mathrm{Re}[Y_{AG}(V_{AG}, \omega)] &= 0 \\ \mathrm{Im}[Y_{AG}(V_{AG}, \omega)] &= 0. \end{aligned} \tag{29}$$

When applying the above procedure to the circuit in Fig. 2(c), we obtain the periodic solution curves in Fig. 9, where they are compared with those resulting from the analytical calculation. As expected, discrepancies are more significant for the higher amplitudes, due to a greater influence of the harmonic terms. When the oscillation amplitude

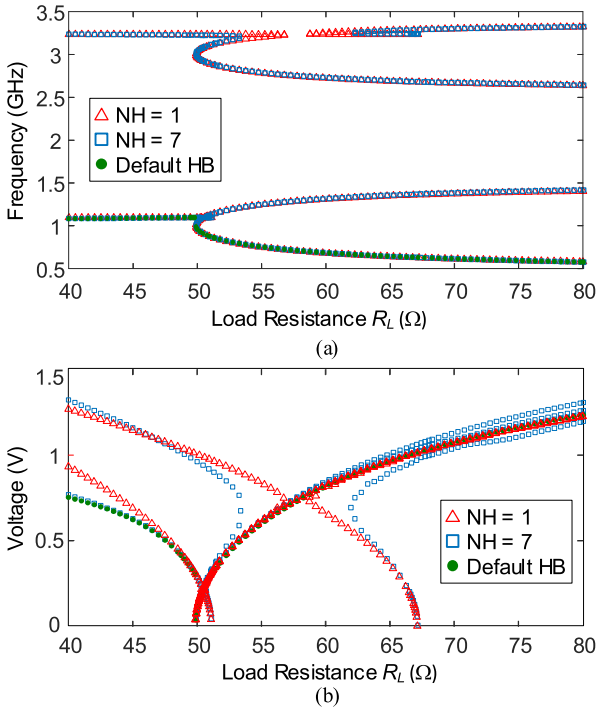

Fig. 9. Comparison of the periodic solution curves obtained with the describing function and with HB, under NH = 7 harmonic terms. Two different kinds of HB analysis are considered: the one based on (29) and oscillator analysis in commercial HB: "Default HB." (a) Frequency. (b) Amplitude.

decreases, the curves obtained with NH = 7 overlap with the analytical calculation. We also present the results of commercial HB, which are superimposed in Fig. 9. The calculated solution points agree with those provided (29), which confirms the accuracy. However, commercial HB jumps between different curve sections, which prevents a correct interpretation of the solution pattern.

We also performed a detailed stability analysis of the periodic curves obtained through HB with NH = 7 harmonic terms (Fig. 9). This analysis is based on pole-zero identification applied to a transfer function calculated with the conversion-matrix approach [19], [20]. In Type-II solutions, this stability analysis detects unstable poles about ω_o and its odd harmonics. In the practical implementation, the higher frequency poles will be removed by the device packaging and other filtering effects. Limiting the identification to a band about ω_o, solutions of Type II at a frequency in the lower (upper) branch exhibit a pair of complex-conjugate poles about the frequency of the upper (lower) branch. Intuitively, the instability of the periodic solutions can be understood from the fact that they do not "make use" of the two pairs of RHS poles of the dc solution.

IV. Quasi-Periodic Oscillations

We will initially perform an analytical calculation of the quasi-periodic oscillations using a double-input describing function. Then, we will carry out an approximate stability analysis. Finally, we will accurately obtain the quasi-periodic oscillations using envelope transient [26] with NH = 7.

A. Analytical Calculation of the Steady-State Solutions

To obtain the quasi-periodic solutions, we will express the voltage across the nonlinear element $i(v)$ in Fig. 2 as $v(t) = V_{q1}\cos(\omega_1 t) + V_{q2}\cos(\omega_2 t)$, where the two frequencies ω_1 and ω_2 are incommensurate. Thus, the phase of the two sinusoidal terms can be arbitrarily set to zero. Next, we will introduce $v(t)$ in the cubic nonlinearity $i(v) = G_N v + bv^3$. Disregarding the intermodulation terms, we obtain the following two nonlinear admittance functions at the respective frequencies ω_1 and ω_2:

$$\begin{aligned} Y_1(V_{q1}, V_{q2}) &= G_N + \frac{3}{4}bV_{q1}^2 + \frac{3}{2}bV_{q2}^2 \\ Y_2(V_{q1}, V_{q2}) &= G_N + \frac{3}{2}bV_{q1}^2 + \frac{3}{4}bV_{q2}^2. \end{aligned} \tag{30}$$

Applying Kirchoff's laws to Node 1 at ω_1 and ω_2, the quasi-periodic oscillations must fulfill

$$\begin{aligned} Y_{T,1} &= Y_1(V_{q1}, V_{q2}) + Y_{\text{in}}(j\omega_1) = 0 \\ Y_{T,2} &= Y_2(V_{q1}, V_{q2}) + Y_{\text{in}}(j\omega_2) = 0. \end{aligned} \tag{31}$$

The equations above should be sufficient to predict sections of the quasi-periodic curves with low amplitude. Splitting (31) into real and imaginary parts, we obtain

$$\begin{aligned} G_{T,1} &= G_N + \frac{3}{4}bV_{q1}^2 + \frac{3}{2}bV_{q2}^2 + Y_{\text{in}}^r(j\omega_1) = 0 \\ B_{T,1} &= Y_{\text{in}}^i(j\omega_1) = 0 \\ G_{T,2} &= G_N + \frac{3}{4}bV_{q2}^2 + \frac{3}{2}bV_{q1}^2 + Y_{\text{in}}^r(j\omega_2) = 0 \\ B_{T,2} &= Y_{\text{in}}^i(j\omega_2) = 0. \end{aligned} \tag{32}$$

From the inspection of (32), the fundamental frequencies of the quasi-periodic solutions are given by the roots of $Y_{\text{in}}^i(j\omega_m) = 0$, where $m = 1, 2$. The corresponding amplitudes are calculated by replacing these roots in $Y_{\text{in}}^r(j\omega_m) = 0$. We should solve the two remaining equations $G_{T,1} = 0$ and $G_{T,2} = 0$ in terms of V_{q1} and V_{q2}. Equation $Y_{\text{in}}^i(j\omega_m) = 0$ is identical to the one used to calculate the periodic solutions: $T_{i1}(\omega)T_{i2}(R_L, \omega) = 0$. Thus, there will also be two kinds of quasi-periodic solutions.

In quasi-periodic solutions of Type I, the frequency ω_1 is a root of $T_{i1}(\omega) = 0$ and ω_2 is a root of $T_{i2}(R_L, \omega)$ or vice versa. Replacing these frequency values in the subsystem of (32) composed of $G_{T,1} = 0$ and $G_{T,2} = 0$, the respective amplitudes V_{q1} and V_{q2} will be different since $Y_{\text{in}}^r(j\omega_1) \neq Y_{\text{in}}^r(j\omega_2)$.

In quasi-periodic solutions of Type II, both ω_1 and ω_2 are roots of $T_{i2}(R_L, \omega)$. As already seen at all the roots of $T_{i2}(R_L, \omega)$, we have $\text{Re}[Y_{\text{in}}(j\omega_m)] = G_L$, so the amplitudes V_{q1} and V_{q2} will be identical. Particularizing (32) to this case

$$\begin{aligned} Y_{T1}^r &= \frac{3}{4}bV_{q1}^2 + \frac{3}{2}bV_{q2}^2 + G_N + G_L = 0 \\ T_{i2}(R_L, \omega_1) &= 0 \\ Y_{T2}^r &= \frac{3}{4}bV_{q2}^2 + \frac{3}{2}bV_{q1}^2 + G_N + G_L = 0 \\ T_{i2}(R_L, \omega_2) &= 0. \end{aligned} \tag{33}$$

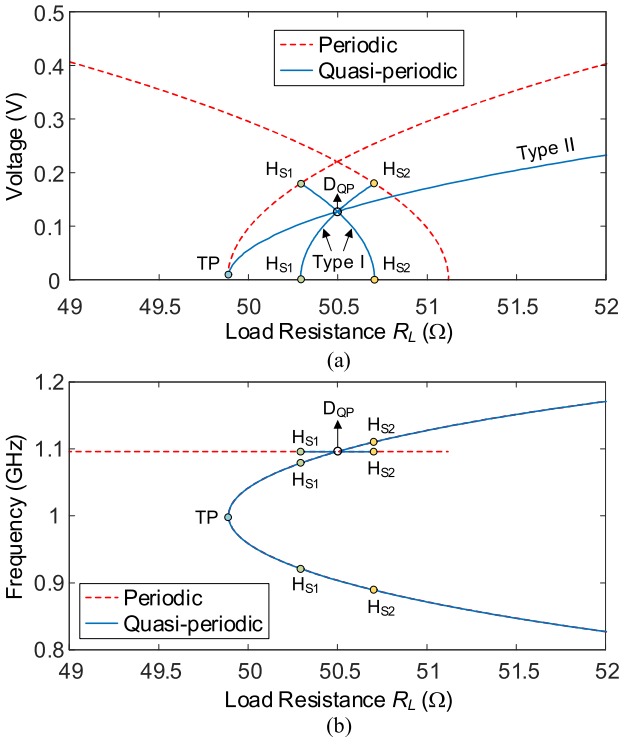

Fig. 10. Evolution versus R_L of the quasi-periodic solutions obtained from (33), in solid line, and the periodic ones obtained from (21), in dashed line. (a) Amplitude variation. (b) Frequency variation.

Solving the above system, the steady-state amplitudes V_{q1} and V_{q2} are equal and given by

$$V_{q1} = V_{q2} = \frac{2}{3}\sqrt{\frac{-(G_N + G_L)}{b}}. \tag{34}$$

The above amplitude can be related to that of the periodic solutions of Type II, given by (23): $V_{q1} = V_{q2} = V/\sqrt{3}$. Thus, the quasi-periodic curves have a lower amplitude.

Fig. 10(a) and (b) shows the evolution of the two types of quasi-periodic solutions versus R_L. For better clarity, we only display the solutions obtained about 1 GHz. The quasi-periodic solutions of Type I are easily distinguished by their different amplitude at ω_1 and ω_2. In fact, they are composed of two distinct subcurves, one at each fundamental frequency (ω_1 and ω_2). They are generated from the periodic curves through secondary Hopf bifurcations (H_s) [16], [21], at which the new spectral linearizes from zero amplitude. The secondary Hopf bifurcation from the periodic solution at ω_1 is obtained by setting $V_{q2} = 0$ in (32) and solving for V_{q1}. The secondary Hopf bifurcation from the periodic solution at ω_2 is obtained by setting $V_{q1} = 0$ in (32) and solving for V_{q2}.

The quasi-periodic solutions of Type II are generated through two different mechanisms, depending on the value of $|R_N|$. For $|R_N| > R_o$, they are generated at the already detected double-Hopf bifurcation, with $\omega_1 \neq \omega_2$. For $|R_N| < R_o$, they are generated at the TP of the Type-II periodic curve. In the latter case, the two fundamental frequencies initially have the difference $\Delta\omega_{21} = |\omega_2 - \omega_1| = 0$, which grows continuously when increasing R_L from the TP. When doing so, the frequencies ω_1 and ω_2 follow the upper and lower sections of the bell-shaped curve, respectively. Due to the fast growth of $\Delta\omega_{21}$ near R_o, quasi-periodic solutions of Type II are the ones with interest for the sensing application proposed in [11].

The intermodulation terms have been neglected in the analytical study. However, in the low amplitude sections, these terms will have a negligible impact. The situation should be like that of Fig. 9, where the curves obtained with the describing function (NH = 1) and HB with NH = 7 overlap in the lower amplitude sections. Thus, near the EPD, the predicted quasi-periodic solution should have a reasonable accuracy.

B. Stability Analysis

For the stability analysis of the quasi-periodic solutions, we will make use of derivations in [27]. This approximate analysis relies on the double-input describing function and considers small amplitude and frequency perturbations about the quasi-periodic steady state. Because we have a system of two complex equations, the linearization provides four eigenvalues. As in any quasi-periodic solution with two autonomous oscillations [28], [29], [30], two of these four eigenvalues are equal to zero (each associated with one of the two oscillations). Then, the stability properties are determined by the two remaining eigenvalues, given by [27]

$$\lambda_{1,2} = \frac{a_{11} + a_{22}}{2} \pm \frac{\sqrt{(a_{11} + a_{22})^2 - 4D}}{2}$$
$$D = a_{11}a_{22} - a_{12}a_{21} \tag{35}$$

where the coefficients a_{ij} are

$$a_{11} = -\left(\frac{\partial G_{T,1}}{\partial V_1}\frac{\partial B_{T,1}}{\partial \omega_1}\right)\Big/\left|\frac{\partial Y_{T,1}}{\partial \omega_1}\right|^2 = -\alpha\bar{B}_{\omega 1}$$
$$a_{12} = -\left(\frac{\partial G_{T,1}}{\partial V_2}\frac{\partial B_{T,1}}{\partial \omega_1}\right)\Big/\left|\frac{\partial Y_{T,1}}{\partial \omega_1}\right|^2 = -2\alpha\bar{B}_{\omega 1}$$
$$a_{21} = -\left(\frac{\partial G_{T,2}}{\partial V_1}\frac{\partial B_{T,2}}{\partial \omega_2}\right)\Big/\left|\frac{\partial Y_{T,2}}{\partial \omega_2}\right|^2 = -2\alpha\bar{B}_{\omega 2}$$
$$a_{22} = -\left(\frac{\partial G_{T,2}}{\partial V_2}\frac{\partial B_{T,2}}{\partial \omega_2}\right)\Big/\left|\frac{\partial Y_{T,2}}{\partial \omega_2}\right|^2 = -\alpha\bar{B}_{\omega 2}. \tag{36}$$

Note that we have particularized the above coefficients to our quasi-periodic solutions of Type II, which fulfill

$$V_{q1} = V_{q2}$$
$$\frac{\partial G_{T,1}(V_{q1}, V_{q2})}{\partial V_1} = \frac{\partial G_{T,2}(V_{q1}, V_{q2})}{\partial V_2} = \alpha$$
$$\frac{\partial G_{T,1}(V_{q1}, V_{q2})}{\partial V_2} = \frac{\partial G_{T,2}(V_{q1}, V_{q2})}{\partial V_1} = 2\alpha. \tag{37}$$

In (36), we have also introduced two normalizations

$$\bar{B}_{\omega 1} = \frac{\frac{\partial B_{T,1}}{\partial \omega_1}}{\left|\frac{\partial Y_{T,1}}{\partial \omega_1}\right|^2}, \quad \bar{B}_{\omega 2} = \frac{\frac{\partial B_{T,2}}{\partial \omega_1}}{\left|\frac{\partial Y_{T,2}}{\partial \omega_2}\right|^2}. \tag{38}$$

Replacing (37) and (38) in (35), a Type-II quasi-periodic solution will be stable if it fulfills the following two conditions:

$$\bar{B}_{\omega 1}\bar{B}_{\omega 2} < 0$$
$$\bar{B}_{\omega 1} + \bar{B}_{\omega 2} > 0. \tag{39}$$

As observed from Fig. 5(a), near R_o (minimum of the bell-shaped curve), the frequency derivative $\partial B_{T,1}/\partial\omega_1$ is positive, whereas $\partial B_{T,2}/\partial\omega_2$ is negative and smaller in absolute value. Thus, the two conditions in (39) are fulfilled. This demonstrates the stability of quasi-periodic solutions of Type II near their generation point. As already stated, this is the targeted solution for the sensing application due to the high sensitivity of $\Delta\omega_{21}$ with respect to R_L near R_o. As R_L increases, the analysis based on the double-input describing function, under the assumption of a small frequency perturbation, progressively becomes invalid. In fact, the steady-state quasi-periodic solution will have intermodulation products disregarded in (32). Instead, the envelope-transient analysis [26] of Section IV-C will consider all the intermodulation terms.

C. Sensitivity to the Load Resistance R_L

At the EPD, we ideally obtain a quasi-periodic solution of Type II, which should fulfill (33) for $V_{q1} = V_{q2} = 0$ and $\omega_1 = \omega_2 = \omega_o$. When slightly increasing R_L from the EPD, the two equal amplitudes will continuously grow from zero. The difference between the two fundamental frequencies $\Delta\omega_{21} = |\omega_2 - \omega_1|$ will also grow from zero with a high sensitivity. Assuming a small resistor increment ΔR_L, the difference $\Delta\omega_{21}$ can be predicted by expanding $T_{i2}(\omega, R_L)$ in a Taylor series about ω_o. As $T_{i2}(\omega_o) = \partial T_{i2}(R_o, \omega_o)/\partial\omega = 0$, we must consider a second-order derivative $\partial^2 T_{i2}(R_o, \omega_o)/\partial\omega^2$. This provides

$$\frac{1}{2}\frac{\partial^2 T_{i2}(\omega_o, R_o)}{\partial\omega^2}(\Delta\omega)^2 = -\frac{\partial T_{i2}(\omega_o, R_o)}{\partial R_L}\Delta R_L. \tag{40}$$

The frequency variation is proportional to the square root of the parameter perturbation, as expected in a second-order EPD [5]. For validation, the results provided by (40) have been compared with the roots of $T_{i2}(\omega)$, calculated versus R_L (Fig. 11). We conclude that the two fundamental frequencies can be predicted with reasonable accuracy from (40), by expressing $\omega_1 = \omega_o - \Delta\omega$ and $\omega_2 = \omega_o + \Delta\omega$. In general terms, the sensitivity increases for a larger L_m and C_m, in comparison with L_0 and C_0. However, an additional fitting is required to set the EPD at the desired value, which will give rise to different sets of parameter values. To illustrate this, we have considered four different sets, fit to provide the same EPD (ω_o, R_o). The results are shown in Fig. 11(b).

D. Numerical Calculation of the Quasi-Periodic Solution

For an accurate numerical calculation of the quasi-periodic solution, we will make use of the envelope-transient method [25]. This analysis is carried out at the circuit level in commercial software (Keysight ADS [24]), which uses a nodal formulation [21]. For a conceptual explanation, we will consider a vector $\bar{x}(t)$, including all the circuit state variables. This is expressed in a Fourier series with time-varying harmonic terms. For the analysis of the EPD oscillator, we will make use of a single fundamental frequency, corresponding to one of the two fundamentals, $f_{1,2} = 1$ GHz $\pm\ \Delta f$, of the

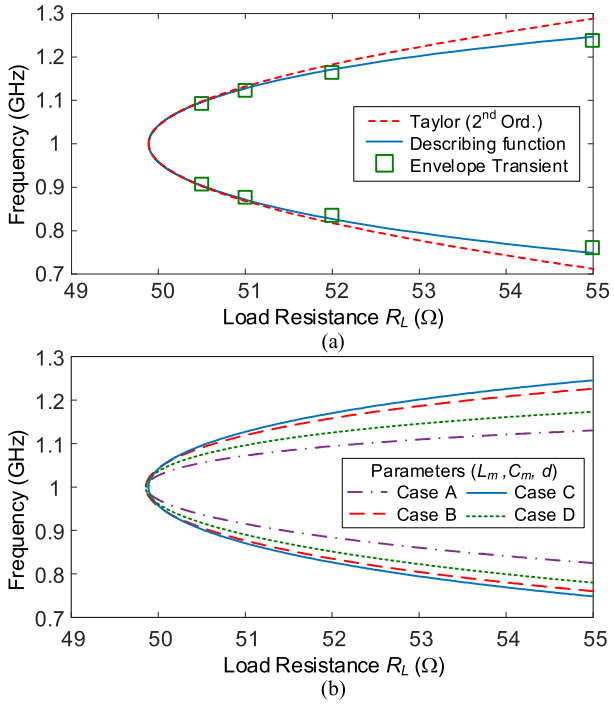

Fig. 11. Sensitivity versus R_L of the two fundamental frequencies of the quasi-periodic solution of Type II. (a) Comparison of the approach (40) with a direct calculation of the roots of $T_{i2}(R_L, \omega) = 0$. (b) Dependence on the parameters, L_m, C_m, and d of the coupled transmission lines. Case A (96.67 nH/m, 452.7 pF/m, and 20 mm), Case B (274.3 nH/m, 216.73 pF/m, and 30 mm), Case C (367.4 nH/m, 102.7 pF/m, and 40.15 mm), and Case D (422.47 nH/m, 37.67 pF/m, and 50 mm), fit to provide the same EPD.

quasi-periodic solution. Taking the positive sign (f_1), $\bar{x}(t)$ is expressed as

$$\bar{x}(t) = \sum_{k=-\mathrm{NH}}^{\mathrm{NH}} \bar{X}_k(t) e^{jk\omega_1 t}. \tag{41}$$

To maintain consistency with the previous analyses, we will set NH = 7. The oscillations are initialized by introducing a small-amplitude current source $I(t)$ at the frequency ω_1. The source is active only during the initial time steps. This is implemented using a conditional statement that sets it to zero after a certain time value: $I(t) = 0$ for $t > t_0$. The integration time step of the envelope analysis [providing the harmonic terms $\bar{X}_k(t)$] must be short enough to accurately predict the additional oscillation at ω_2. It should be able to capture the frequency difference $\Delta\omega_{21}$, as well as the intermodulation terms between ω_1 and ω_2.

For the first analysis, we have taken $-R_N = 49.88\ \Omega$. The resulting spectrum, centered about $(\omega_1 + \omega_2)/2$, is shown in Fig. 12(a). There are two fundamental frequencies, with approximately the same amplitude, in agreement with [11] and [12] and the analyses of Section III-A. As R_L increases, the difference $\Delta\omega_{21}$ between the two fundamental frequencies increases too. The frequencies obtained with this independent envelope-transient simulation, superimposed in Fig. 11, exhibit an excellent agreement with the analytical predictions.

For the second analysis, we have taken $R_N = -51\ \Omega$ [Fig. 12(b)]. It fulfills $|R_N| > R_o$, so the quasi-periodic solution should start with a frequency difference $\Delta\omega_{21} = |\omega_2 - \omega_1| \neq 0$ [like in Fig. 7(a)], at a double-Hopf bifurcation.

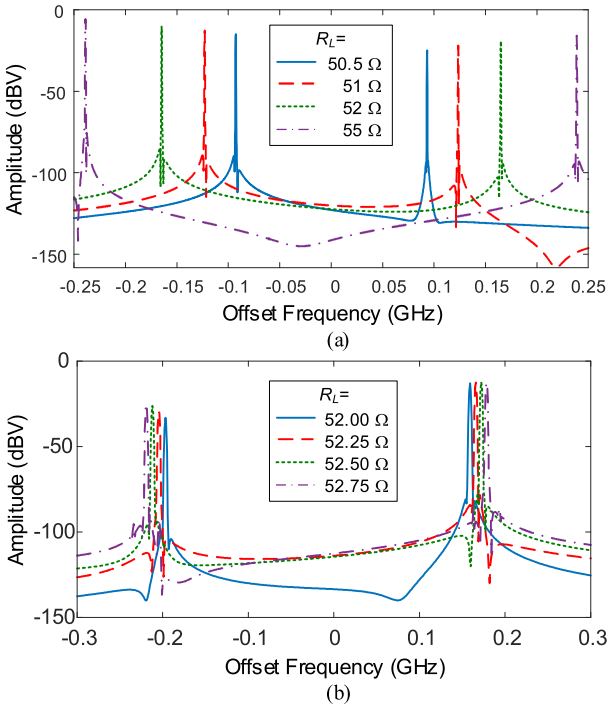

Fig. 12. Envelope-transient analysis of the quasi-periodic solutions. (a) For $R_N = -49.88\ \Omega$ and several R_L values. (b) For $R_N = -51\ \Omega$ and several R_L values.

Because it arises at a certain R_L distance from the minimum of $T_{i2}(R_L, \omega) = 0$, the difference $\Delta\omega_{21}$ grows more slowly than in the case of $R_N = -49.88\ \Omega$ [Fig. 12(a)]. This quasi-periodic solution is generated at a double-Hopf bifurcation, so the amplitudes of its two fundamental spectral lines start from zero [Fig. 7(b)]. This explains the smaller amplitudes obtained for $R_N = -51\ \Omega$ [Fig. 12(b)] in comparison with $R_N = -49.88\ \Omega$ [Fig. 12(a)].

In conclusion, the EPD is a degenerate double-Hopf bifurcation at which a quasi-periodic solution arises at the two fundamental frequencies $\omega_1 = \omega_2 = \omega_o$. In practice, we must ensure $|R_N| < R_o$, with $|R_N| \cong R_o$. This will provide a quasi-periodic solution, arising with zero difference between the two fundamental frequencies $\Delta\omega_{21} = |\omega_2 - \omega_1| = 0$. The two frequencies, ω_1 and ω_2, split with a high sensitivity to the parameter, acting as the measurand, as desired for the sensing application. In the second stage, the designer should carry out an envelope-domain analysis to obtain this quasi-periodic solution and evaluate its sensitivity in fully nonlinear conditions.

V. Practical Implementation and Measurement Results

As demonstrated in numerous previous works [31], [32], [33], [34], [35], [36], the cubic nonlinearity $i = G_N v + bv^3$ can be implemented with a pair of cross-coupled transistors. However, this configuration is balanced. For the transition to a single-ended one, here we have made use of a Marchand balun [16], which enables a planar implementation (Fig. 13). The transistors are ATF34143. The biasing and terminations are chosen to best fit the cubic nonlinearity considered in the

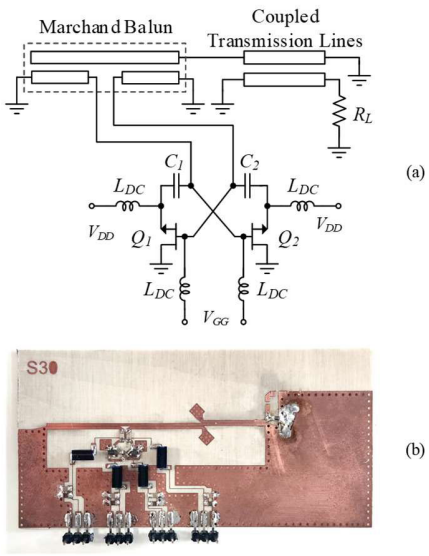

Fig. 13. Implemented oscillator. (a) Schematic. (b) Photograph.

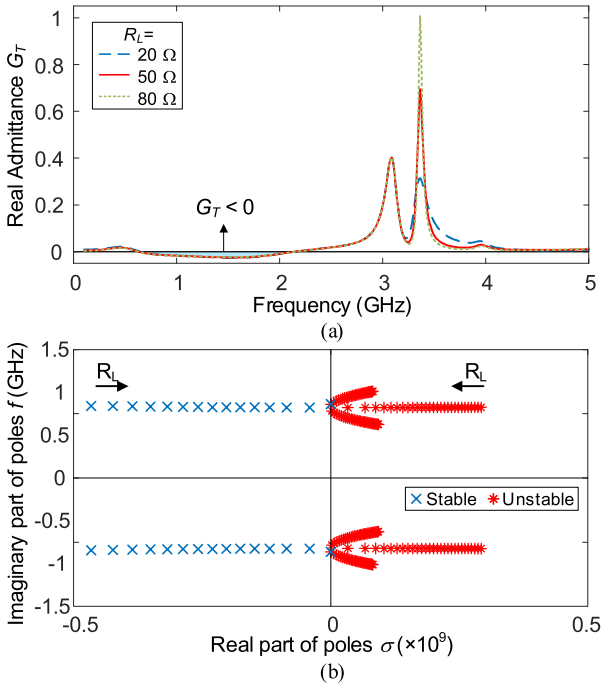

Fig. 14. Oscillator based on cross-coupled transistors. (a) Real part of the input admittance. (b) Pole variation after compensating for dispersion and parasitics.

analytical study. The variation of the small-signal conductance, fit to $G_N = -1/49.88$ S in a broad frequency band about 1 GHz, is shown in Fig. 14(a). The positive conductance of about 3 GHz suppresses the additional oscillations about the odd harmonics. We have used the graphical method based on plotting $G_T(G_L, \omega) = 0$ and $T_{i2}(\omega, R_L) = 0$ to compensate for dispersion and parasitic effects, which has been achieved through the tuning of the bias voltage and bias network. The resulting pole locus [Fig. 14(b)] exhibits the expected structure.

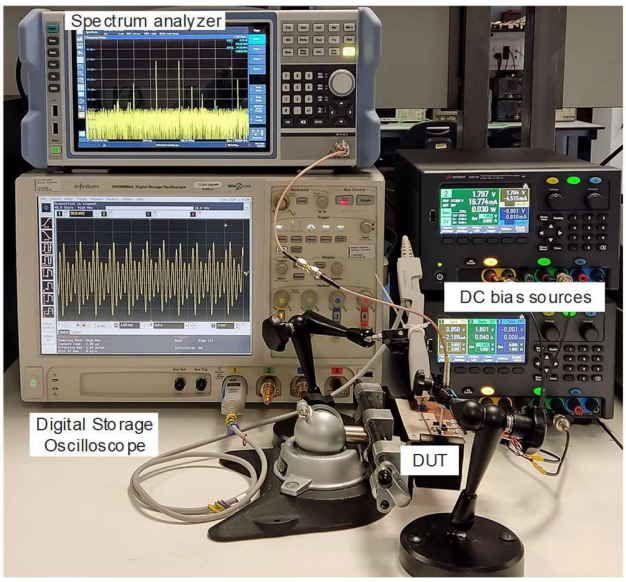

Fig. 15. Experimental characterization setup, composed of an oscilloscope paired with an active probe and a spectrum analyzer equipped with a monopole antenna.

The setup for the experimental characterization is shown in Fig. 15. It comprises an Infiniium Digital Storage Oscilloscope (DSO90404A) paired with a 1134A InfiniiMax 7 GHz high-impedance active probe. The scope enables a fast, dynamic, and efficient evaluation of the waveforms at different nodes. The high-frequency resistors that act as the measurand are connected to the resistive termination of the coupled transmission lines. The circuit operation was validated with the noncontact RF probe before using the active probe. The position of the probe, as well as its orientation and distance to the board, has been set to minimize any possible influence on the desired operation mode. Because the resistive termination is employed for that purpose, the spectrum is measured with the aid of a monopole antenna constructed using RG316 coaxial cable, which is connected to the spectrum analyzer. The monopole antenna serves as a contactless passive probe for capturing the oscillator spectrum without disturbing the circuit symmetries. The sensing is based on the variation of the frequency difference between the two fundamentals of the quasi-periodic solution, so this procedure enables a reliable characterization. To ensure precise positioning, 3-D probe positioners are utilized for both the active probe and the monopole antenna. In this way, we have obtained the oscillator spectrum when loading the coupled lines with several surface-mount device (SMD) thick-film resistors (0603 and 0805) usable at high frequency. We have considered the available commercial values $R_L = 47$, 51, 56, and 62 Ω. Fig. 16(a) shows the experimental spectra obtained for $R_L = 47$ and 62 Ω. As can be seen, the qualitative behavior is very similar to the one obtained in the simulations in Fig. 12. The response in terms of the frequency difference $\Delta\omega_{21}$ exhibits good agreement with the analysis results. It is measured as the difference between the frequencies of the two central spectral lines (having the highest output power), indicated with arrows. This can be seen in Fig. 16(b), where Δf_{21} has been represented

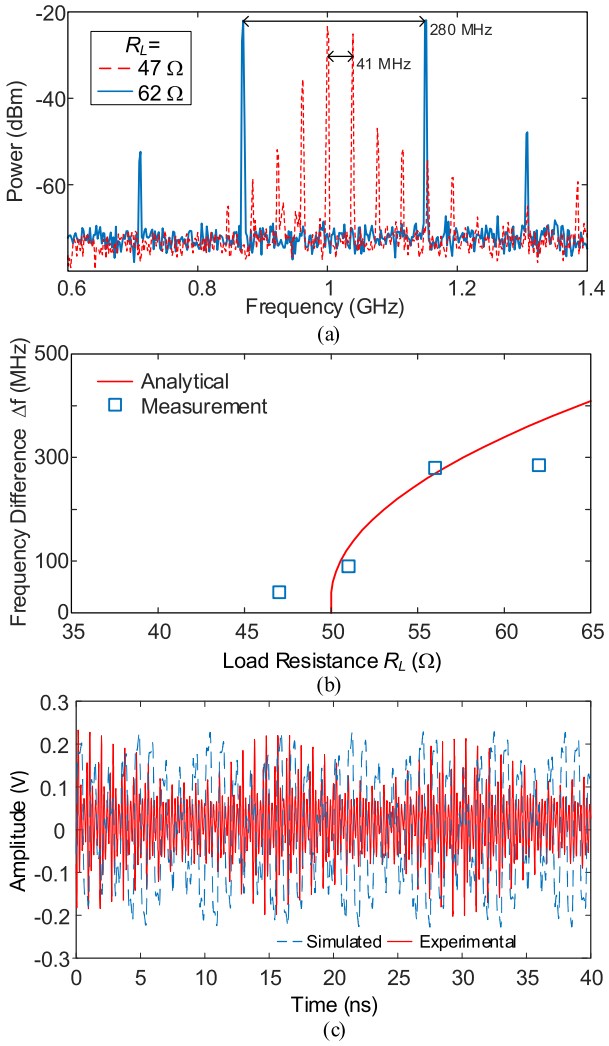

Fig. 16. Experimental results for the available commercial resistors. (a) Spectra obtained for $R_L = 47$ and 62 Ω. (b) Difference between the two fundamental frequencies, $|\Delta f_{21}|$, versus the load resistor R_L, compared with the analysis results. (c) Comparison between the simulated and experimental waveforms.

versus the resistor R_L. Fig. 16(c) compares the simulated and experimental quasi-periodic waveforms. The amplitude limits are approximately the same in measurement and simulation. Due to the existence of two Lyapunov exponents equal to zero, the solution has a double autonomy. We must keep in mind that the simulation was carried out using a cubic-nonlinearity model for the active device, whereas the manufactured circuit is based on two cross-coupled transistors.

VI. Conclusion

An in-depth investigation of an oscillator based on finite-length coupled transmission lines with nearly balanced gain and loss has been presented. We have proposed a new method for the graphical detection of the EPD. This is based on the representation of the zero-value contours of the real and imaginary parts of total admittance at the analysis node. The oscillatory solutions have been analytically obtained using the described function. There are two different kinds of periodic and quasi-periodic solutions. The one used for the

sensing application is quasi-periodic and ideally generated at the EPD. This corresponds to a degenerate double-Hopf bifurcation with zero difference between the fundamental frequencies. In practice, the quasi-periodic solution can be generated either from zero amplitude and nonzero frequency difference or the opposite: from nonzero amplitude and zero frequency difference. In the latter case, the frequencies will split with high sensitivity to the parameters, as desired for the sensing application. Dispersion and losses in the coupled transmission line do not prevent the occurrence of the EPD; however, it is necessary to counteract these effects. This can be achieved with a new method based on the representation of the zero-value contours of the total admittance. All the results were validated using HB and envelope-transient analyses. We have implemented the oscillator using two cross-coupled transistors loaded with the coupled transmission lines. We observed good agreement between simulated and experimental results.

REFERENCES

[1] H. Kazemi et al., "Ultra-sensitive radio frequency biosensor at an exceptional point of degeneracy induced by time modulation," *IEEE Sensors J.*, vol. 21, no. 6, pp. 7250–7259, Mar. 2021.

[2] T. Mealy and F. Capolino, "General conditions to realize exceptional points of degeneracy in two uniform coupled transmission lines," *IEEE Trans. Microw. Theory Techn.*, vol. 68, no. 8, pp. 3342–3354, Aug. 2020.

[3] M. A. K. Othman and F. Capolino, "Theory of exceptional points of degeneracy in uniform coupled waveguides and balance of gain and loss," *IEEE Trans. Antennas Propag.*, vol. 65, no. 10, pp. 5289–5302, Oct. 2017.

[4] G. W. Hanson, A. B. Yakovlev, M. A. K. Othman, and F. Capolino, "Exceptional points of degeneracy and branch points for coupled transmission lines—Linear-algebra and bifurcation theory perspectives," *IEEE Trans. Antennas Propag.*, vol. 67, no. 2, pp. 1025–1034, Feb. 2019.

[5] M. Y. Nada, T. Mealy, and F. Capolino, "Frozen mode in three-way periodic microstrip coupled waveguide," *IEEE Microw. Wireless Compon. Lett.*, vol. 31, no. 3, pp. 229–232, Mar. 2021.

[6] M. Y. Nada, M. A. K. Othman, F. Yazdi, D. Oshmarin, A. F. Abdelshafv, and C. Filippo, "Unique charactersitics and applications of systems with exceptional points of degeneracy," in *Proc. IEEE Int. Symp. Antennas Propag. USNC/URSI Nat. Radio Sci. Meeting*, Boston, MA, USA, Jul. 2018, pp. 869–870.

[7] M. Y. Nada et al., "Microwave circuits with exceptional points and applications in oscillators and sensors," in *Proc. 18th Medit. Microw. Symp. (MMS)*, Istanbul, Turkey, Oct. 2018, pp. 108–111.

[8] E. M. Renzi, A. F. Abdelshafy, T. Mealy, L. Matekovits, and F. Capolino, "A concept for a leaky wave antenna oscillator with second order degeneracy," in *Proc. IEEE Int. Symp. Antennas Propag. North Amer. Radio Sci. Meeting*, Montreal, QC, Canada, Jul. 2020, pp. 147–148.

[9] A. F. Abdelshafy, M. Othman, D. Oshmarin, M. Y. Nada, and F. Capolino, "Exceptional points of degeneracy in a linear array oscillator with gain and loss balance," in *Proc. IEEE Int. Symp. Antennas Propag. USNC/URSI Nat. Radio Sci. Meeting*, Boston, MA, USA, Jul. 2018, pp. 1489–1490.

[10] A. Nikzamir and F. Capolino, "Highly sensitive coupled oscillator based on an exceptional point of degeneracy and nonlinearity," *Phys. Rev. Appl.*, vol. 18, no. 5, pp. 54–59, Nov. 2022.

[11] H. Kazemi, A. Nikzamir, T. Mealy, A. Abdelshafy, and F. Capolino, "High-sensitive parity-time symmetric oscillator in coupled transmission lines with nonlinear gain," *IEEE J. Microw.*, vol. 2, no. 3, pp. 389–400, Jul. 2022.

[12] A. Nikzamir, H. Kazemi, T. Mealy, and F. Capolino, "Highly sensitive exceptional degeneracy in coupled transmission lines with balanced gain and loss," in *Proc. United States Nat. Committee URSI Nat. Radio Sci. Meeting (USNC-URSI NRSM)*, Boulder, CO, USA, Jan. 2022, pp. 55–56.

[13] K. Kurokawa, "Some basic characteristics of broadband negative resistance oscillator circuits," *Bell Syst. Tech. J.*, vol. 48, no. 6, pp. 1937–1955, Jul. 1969.

[14] J. Guckenheimer and P. Holmes, *Nonlinear Oscillations, Dynamical Systems, and Bifurcations of Vector Fields*. New York, NY, USA: Springer, 2002.

[15] V. Ardila, F. Ramirez, and A. Suárez, "Analysis and design of injection-locked oscillators coupled to an external resonator," *IEEE Trans. Microw. Theory Techn.*, vol. 71, no. 10, pp. 4546–4561, Oct. 2023.

[16] H. Kawakami, "Bifurcation of periodic responses in forced dynamic nonlinear circuits: Computation of bifurcation values of the system parameters," *IEEE Trans. Circuits Syst.*, vol. CS-31, no. 3, pp. 248–260, Mar. 1984.

[17] V. Rizzoli and A. Neri, "State of the art and present trends in nonlinear microwave CAD techniques," *IEEE Trans. Microw. Theory Techn.*, vol. MTT-36, no. 2, pp. 343–356, Feb. 1988.

[18] R. Schwindt and C. Nguyen, "Computer-aided analysis and design of a planar multilayer Marchand balun," *IEEE Trans. Microw. Theory Techn.*, vol. 42, no. 7, pp. 1429–1434, Jul. 1994.

[19] J. Jugo, J. Portilla, A. Anakabe, A. Suarez, and J. M. Collantes, "Closed-loop stability analysis of microwave amplifiers," *Electron. Lett.*, vol. 37, no. 4, pp. 226–228, 2001.

[20] J.-M. Collantes et al., "Pole-zero identification: Unveiling the critical dynamics of microwave circuits beyond stability analysis," *IEEE Microw. Mag.*, vol. 20, no. 7, pp. 36–54, Jul. 2019.

[21] A. Suárez, *Analysis and Design of Autonomous Microwave Circuits*. Hoboken, NJ, USA: Wiley, 2009.

[22] M. Kirschning and R. H. Jansen, "Accurate wide-range design equations for the frequency-dependent characteristic of parallel coupled microstrip lines," *IEEE Trans. Microw. Theory Techn.*, vol. MTT-32, no. 1, pp. 83–90, Jan. 1984.

[23] A. Gelb and W. Vander-Velde, *Multiple-Input Describing Functions and Nonlinear System Design*. New York, NY, USA: McGraw-Hill, 1968.

[24] *Advanced Design System ADS2022*, Keysight Technol., Santa Rosa, CA, USA, 2024. Accessed: May 7, 2024. [Online]. Available: https://www.keysight.com

[25] A. Suarez, J. Morales, and R. Quere, "Synchronization analysis of autonomous microwave circuits using new global-stability analysis tools," *IEEE Trans. Microw. Theory Techn.*, vol. 46, no. 5, pp. 494–504, May 1998.

[26] E. Ngoya and R. Larcheveque, "Envelop transient analysis: A new method for the transient and steady state analysis of microwave communication circuits and systems," in *IEEE MTT-S Int. Microw. Symp. Dig.*, San Francisco, CA, USA, Jun. 1996, pp. 1365–1368.

[27] F. Ramírez, S. Sancho, and A. Suárez, "Oscillation modes in multiresonant oscillator circuits," *IEEE Trans. Microw. Theory Techn.*, vol. 64, no. 12, pp. 4660–4675, Dec. 2016.

[28] T. Parker and L. Chua, *Practical Numerical Algorithms for Chaotic Systems*. New York, NY, USA: Springer, 1989.

[29] A. Demir, A. Mehrotra, and J. Roychowdhury, "Phase noise in oscillators: A unifying theory and numerical methods for characterization," *IEEE Trans. Circuits Syst. I, Fundam. Theory Appl.*, vol. 47, no. 5, pp. 655–674, May 2000.

[30] F. X. Kaertner, "Analysis of white and f-α noise in oscillators," *Int. J. Circuit Theory Appl.*, vol. 18, pp. 485–519, Mar. 1990.

[31] N. Deparis, A. Siligaris, P. Vincent, and N. Rolland, "Ultra low consumption UWB pulsed-ILO RF front-end transmitter at 60 GHz in 65-nm CMOS-SOI," in *Proc. IEEE 20th Int. Symp. Pers., Indoor Mobile Radio Commun.*, Sep. 2009, pp. 1652–1656.

[32] C. Jany, A. Siligaris, P. Vincent, and P. Ferrari, "A novel approximated solution for the van der pol oscillator. Application to pulsed oscillations modeling in switched cross-coupled MOS oscillators," in *Proc. IEEE 57th Int. Midwest Symp. Circuits Syst. (MWSCAS)*, College Station, TX, USA, Aug. 2014, pp. 745–748.

[33] C. Jany, A. Siligaris, J. L. Gonzalez-Jimenez, P. Vincent, and P. Ferrari, "A programmable frequency multiplier-by-29 architecture for millimeter wave applications," *IEEE J. Solid-State Circuits*, vol. 50, no. 7, pp. 1669–1679, Jul. 2015.

[34] I. Dumitrescu, M. Iordache, L. Dumitriu, L. Mandache, D. Cordeau, and J.-M. Paillot, "Sensitivity and tolerance analysis for oscillator circuits simulated by van der Pol models," in *Proc. 13th Int. Conf. Optim. Electr. Electron. Equip. (OPTIM)*, Brasov, Romania, May 2012, pp. 171–177.

[35] M. Izabela Ionita, D. Cordeau, J. M. Paillot, and M. Iordache, "Analysis and design of an array of two differential oscillators coupled through a resistive network," in *Proc. 20th Eur. Conf. Circuit Theory Design (ECCTD)*, Aug. 2011, pp. 73–76.

[36] I. Dumitrescu, L. Dumitriu, M. Iordache, D. Cordeau, and J.-M. Paillot, "A cad tool for automatic formulation of symbolic state equations of oscillating circuits," in *Proc. Int. Conf. Synth., Model., Anal. Simul. Methods Appl. Circuit Design (SMACD)*, Seville, Spain, Sep. 2012, pp. 289–292.

Camilo Moncada (Student Member, IEEE) was born in Bucaramanga, Santander, Colombia. He received the Professional Career degree in electronic engineering from Santander's Industrial University of Bucaramanga (UIS), Bucaramanga, in 2010, and the M.Sc. degree from Pontificia Javeriana University, Bogotá, Colombia, in 2016. He is currently pursuing the Ph.D. degree in information technology and communications in mobile networks at the University of Cantabria (UC), Santander, Spain.

His research interests include the design and analysis of nonlinear circuits and RF/microwave systems.

Franco Ramírez (Senior Member, IEEE) received the Licentiate degree in electronic systems engineering from the Military School of Engineering (EMI), La Paz, Bolivia, in 2000, and the Ph.D. degree in communications engineering from the University of Cantabria, Santander, Spain, in 2005.

From 1999 to 2000, he worked at Ericsson de Bolivia Telecomunicaciones, La Paz, where he was involved in projects related to global system for mobile communications (GSM) and time-division multiple access (TDMA) technologies. From 2009 to 2013, he was a Research Fellow of the "Ramón y Cajal" Program, funded by the Spanish Ministry of Science and Innovation, at the Communications Engineering Department, University of Cantabria, where he is currently an Associate Professor. His research interests include phase noise, stability, and the development of nonlinear techniques for the analysis and design of autonomous microwave circuits.

Almudena Suárez (Fellow, IEEE) was born in Santander, Spain. She received the Licentiate degree in electronic physics and the Ph.D. degree from the University of Cantabria, Santander, in 1987 and 1992, respectively, and the Ph.D. degree in electronics from the University of Limoges, Limoges, France, in 1993.

She has authored the book *Analysis and Design of Autonomous Microwave Circuits* (IEEE-Wiley, 2009) and co-authored the book *Stability Analysis of Nonlinear Microwave Circuits* (Artech House, 2003).

Prof. Suárez was a member of the Board of Directors of European Microwave Association (EuMA) from 2012 to 2020. She is a member of the TPRCs of the IEEE International Microwave Symposium and European Microwave Week. She received the Research Award of the Social Council of the University of Cantabria in 2021. She was an IEEE Distinguished Microwave Lecturer from 2006 to 2008. She was the Coordinator of the Communications and Electronic Technology Area for the Spanish National Evaluation and Foresight Agency (ANEP) from 2009 to 2013. She was the Chair of the 2014 and 2015 Editions of the IEEE Topical Conference on RF/Microwave Power Amplifiers (PAWR), in Newport Beach and San Diego. She was the General TPC Chair of EuMW 2018. She was the Editor-in-Chief of the *International Journal of Microwave and Wireless Technologies* of Cambridge University Press journals from 2013 to 2018 and an Associate Editor of *IEEE Microwave Magazine* from 2014 to 2022. She was the Chair of the IEEE Subcommittee for the Best Paper Award in *IEEE Microwave Magazine* from 2017 to 2022. She has been the Publication Officer of EuMA since 2021. Since October 2022, she has been the Editor-in-Chief of IEEE TRANSACTIONS ON MICROWAVE THEORY AND TECHNIQUES.